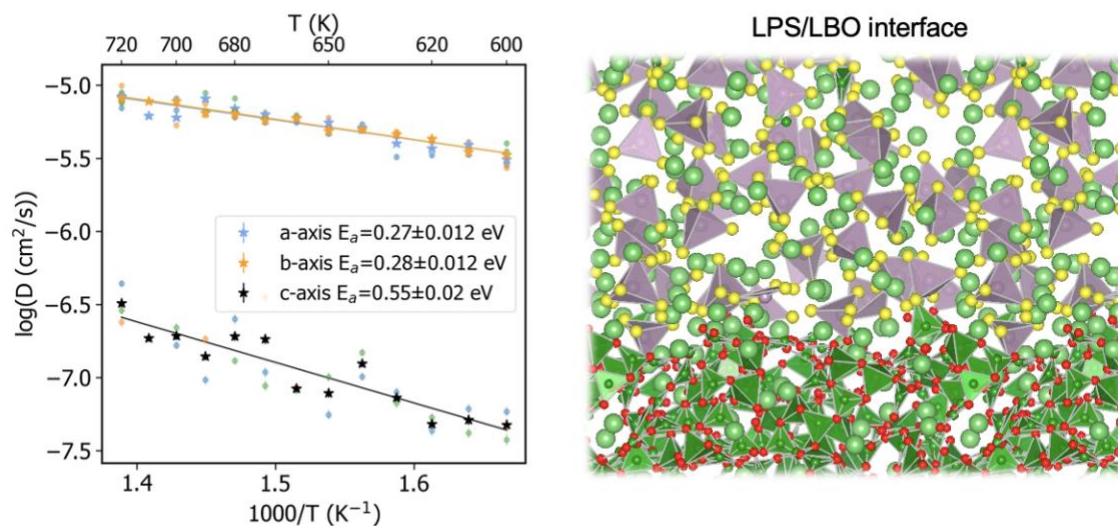# Nature of the amorphous-amorphous interfaces in solid-state batteries revealed using machine-learned interatomic potentials

Chuhong Wang,[1] Muratahan Aykol,[2] Tim Mueller[1,*]

[1] Department of Materials Science and Engineering, Johns Hopkins University, Baltimore, Maryland 21218, United States

[2] Toyota Research Institute, Los Altos, California 94022, United States

*Corresponding Author
Tim Mueller
Department of Materials Science and Engineering
Johns Hopkins University
3400 N. Charles St.
Baltimore, MD 21218 USA
(410)516-5779
tmueller@jhu.edu

Abstract

Non-crystalline solid materials have attracted growing attention in energy storage for their desirable properties such as ionic conductivity, stability and processability. However, compared to bulk crystalline materials, fundamental understanding of these highly complex metastable systems is hindered by the scale limitations of density functional theory (DFT) calculations and resolution limitations of experimental methods. To fill the knowledge gap and guide the rational design of amorphous battery materials and interfaces, we present a molecular dynamics (MD) framework based on machine-learned interatomic potentials trained on the fly to study the amorphous solid electrolyte Li_3PS_4 and its protective coating, amorphous $Li_3B_{11}O_{18}$. The use of machine-learned potentials allows us to simulate the materials at time and length scales that are not accessible to DFT while maintaining a near-DFT level of accuracy. This approach allows us to calculate amorphization energies, amorphous-amorphous interface energies, and the impact of the interface on lithium ion conductivity. This study demonstrates the promising role of actively-learned interatomic potentials in extending the application of ab-initio modeling to more complex and realistic systems such as amorphous materials and interfaces.

Introduction

Li-ion batteries have revolutionized the portable electronics industry.[1] All-solid-state Li-ion batteries employing nonflammable solid electrolytes are attracting growing attention due to their enhanced safety and higher energy density.[2-4] Although several classes of inorganic solid electrolytes with high ionic conductivity have been identified, the performance of all-solid-state batteries is often compromised by interfacial side reactions.[5-9] At present, a major challenge facing all-solid-state batteries is developing materials that enable high mobility of lithium ions in the bulk as well as across interfaces.[10, 11]

Computation has become an important approach for advancing material research for batteries.[12, 13] Density functional theory (DFT) has been particularly successful in evaluating thermodynamic stability, providing bounds for electrochemical stability windows, predicting ionic diffusion mechanisms, and guiding interface engineering.[14-16] In recent years, high-throughput computational screening over wide chemical spaces has emerged as a valuable tool to improve upon experimental trial and error.[16] Simulations of specific material structures have provided insights on atomic and electronic scales, thus aiding the interpretation of experimental observations.[17, 18] Due to the computational cost of DFT calculations, currently most atomic-level studies of materials focus on crystalline materials.[19]

State-of-the-art solid electrolytes are comprised of crystals, glass-ceramics and glasses.[3, 20] Inducing disorder into the structure has emerged as a potential route to enhance the rate of ionic conduction.[21, 22] Compared to crystalline structures, the amorphous counterparts could provide percolation pathways and avoid problems with lattice mismatch, contributing to improved rate capability and long-term cyclability. As opposed to energetically favorable migration paths in

particular directions characterized in various crystalline lithium borate materials,[23] the diffusion rate of charge carriers in the amorphous phase is independent of its orientation, which facilitates processing to achieve the theoretical rate capability. The benefits of non-crystalline materials are reflected in the fact that many state-of-the-art coatings used in batteries, including $LiNbO_3$, $LiTaO_3$, Li_4GeO_4, Li_3PO_4, Al_2O_3, $Li_{3.5}Si_{0.5}P_{0.5}O_4$, and lithium borate obtained by various preparation methods, exhibit low crystallinity in experimental characterizations.[24-30] Despite the increasing interest in using amorphous materials as solid electrolytes and electrode coatings,[31-33] relatively little is known about the interfacial properties and atomistic mechanisms of ionic diffusion in these materials, leaving a gap in our knowledge of how to improve cycling performance in batteries with amorphous materials. This is in part due to the challenge of using experimental methods to accurately characterize atomic structures of amorphous materials.[34]

First-principles modeling of amorphous structures is challenging because unlike crystals, amorphous structures lack translational symmetry. It is thus necessary to use large simulation cells which can be prohibitively expensive to model, especially if long time scales are required. Ab-initio molecular dynamics (AIMD) has been used in several studies on solid electrolyte materials with high lithium ion conductivity,[35-37] but there have only been a few reported studies that simulated amorphous coatings, and these were mainly done with empirically parametrized models such as classical force-field-based molecular dynamics simulations and Monte Carlo annealing.[37-39] It is a non-trivial task to develop interatomic potentials for new glass chemistries, and it becomes even more challenging for highly complex systems such as amorphous-amorphous interfaces. To circumvent the limitation of inaccurate empirical interatomic potentials, other approaches have been employed to construct atomistic models for disordered and heterogeneous systems including reverse Monte Carlo modeling (RMC)[40] and hybrid reverse Monte Carlo algorithm (HRMC)[41] which combines RMC with molecular dynamics (MD). Although these methods can be effective, they require experimental diffraction data which is not always readily available.

Machine learning has proven to be versatile for circumventing the limitations of first principles calculations, facilitating the prediction of materials properties that are otherwise hard to access.[42-45] In our previous work, we developed a screening scheme for solid-state ionic conductors based on active learning of moment tensor potential (MTP) models and achieved better agreement with experimentally-determined activation energies than what could be achieved by DFT alone.[46-48] In this scheme, structures that are significantly different from those used to train the potential are identified on the fly during MD and added to the training set, preserving the accuracy of the machine-learned potential and minimizing the cost of generating training data. Such an active learning scheme is also promising for amorphous materials, as it provides accuracies close to that of DFT but allows simulations on much longer time and length scales. In this work, combining the capability of first principle methods to accurately treat arbitrary configurations with the high speed of machine-learned interatomic potential models, we present an active learning scheme to achieve accurate atomistic modeling of amorphous materials. We demonstrate this scheme by applying it to the commonly employed amorphous solid electrolyte Li_3PS_4 and the novel amorphous protective coating $Li_3B_{11}O_{18}$.[30]

While most simulations on battery materials so far have studied bulk structures, understanding the atomic dynamics across interfaces is critical to improving the cycling performance of all-solid-state batteries.[49] Due to the unique chemical environment at the interface, ionic dynamics in its vicinity may differ from that in the constituent phases on either side. It is non-trivial to estimate the conduction rate or the diffusion mechanism across the interface even when both bulk materials are well characterized. Recently several DFT studies have examined the geometry and electronic properties of systems such as Li/Li_2O, Li/Li_3PS_4, $Li/Li_7La_3Zr_2O_{12}$, $Li/LiPON$ on the anode side[50-52] and $LiCoO_2/Li_3PS_4$, $LiFePO_4/Li_3PS_4$ on the cathode side.[53, 54] Among those studies, a few reported diffusion activation energies across crystalline interfaces by performing climbing-image nudged elastic band (CI-NEB)[55, 56] calculations with a manually determined diffusion paths.[52, 54] Such an approach could be very challenging for amorphous materials due to their high structural complexity, wide variety of local atomic environments, and cooperative atomic motions involved in diffusion. To address this challenge, we extend our active learning-driven MD study to investigate the atomic structure and ionic diffusion at the amorphous-amorphous interface between $Li_3B_{11}O_{18}$ and Li_3PS_4. This approach enables us to predict the interfacial energy between two amorphous ionic compounds, which is rarely found in literature. We further quantify the effect of the interface on the overall ionic conductivity of the coated solid electrolyte. The result provides atomic-scale insights into the experimentally-observed enhanced rate performance by the borate coating.[30]

Methods

1. Molecular dynamics

Ab-initio MD simulations were performed using the Perdew-Burk-Ernzerhof (PBE) generalized gradient approximation exchange-correlation functional[57] and projector augmented wave[58] potentials (PAW_PBE Li, PAW_PBE P, PAW_PBE S, PAW_PBE B and PAW_PBE O) using the Vienna Ab initio Simulation Package (VASP).[59, 60] We used a plane wave energy cut-off of 400 eV and a minimal Γ-centered $1 \times 1 \times 1$ k-point mesh which has been shown to provide a satisfactory balance between computational accuracy and cost in large systems.[61, 62] Non-spin-polarized calculations were performed. A time step of 2 fs was adopted for MD. The temperature control for NVT-AIMD simulations and NPT-AIMD simulations was achieved by using a Nosé-Hoover thermostat with a Nosé-mass corresponding to a period of 40 time steps (SMASS=0)[63, 64] and Langevin thermostat[65, 66] respectively.

Our learning on-the-fly (LOTF)-MD scheme automatically switches between MTP-MD in LAMMPS[67] and DFT retraining in VASP. During the dynamic evolution of the structure in MTP-MD, MTP re-training was conditionally activated by the occurrence of an "extrapolating" configuration as determined by the D-optimality criterion,[68] corresponding to the *extrapolation grade[69]* parameter coded in MLIP. The MPT-MD was terminated once the extrapolation grade exceeded the selection threshold, which we set to 10, consistent with recent publications.[46]

Structures that had extrapolation grades above 1.5 were selected from the MD trajectory to be added to the DFT training set. The MTP was re-trained on the updated training set and MTP-MD run was restarted with the new potential. The active learning process was managed by the Machine Learning of Interatomic Potentials (MLIP) software package.[69] The MTP cutoff radius and the maximum level of basis functions, lev$_{max}$ were chosen to be 5.0 Å and 12, respectively. MTP-MD simulations in the isothermal-isobaric (NPT) ensemble used the Nose-Hoover thermostat and barostat.[64, 70] The Nose-Hoover thermostat was also used to maintain the temperature in the canonical (NVT) ensemble. We applied a time step of 2 fs in LAMMPS, consistent with that used in AIMD. Details of the active learning criteria, DFT validation error of energies and forces on various crystalline structures as well as experimental benchmark results on diffusion barrier energy prediction can be found in our previous publication.[46]

2. Workflow

The initial structures of bulk glasses were constructed by randomly distributing Li atoms and PS4 tetrahedral units (96 atoms in total) in 12 Å × 12 Å × 14.87 Å simulation boxes for Li_3PS_4, and Li, B and O atoms (128 atoms in total) in 12 Å × 12 Å × 10.64 Å simulation boxes for $Li_3B_{11}O_{18}$, to match the densities of their crystalline counterparts.[71, 72] Interface structures were initialized by stacking randomly initialized bulk components. The vertical displacements of the top component were adjusted within the range of 1.2~1.5 Å to ensure Li-Li distance of at least 2.5 Å. We obtained an ensemble of four independently initialized structures for each composition of bulk materials and the solid-solid interfaces.
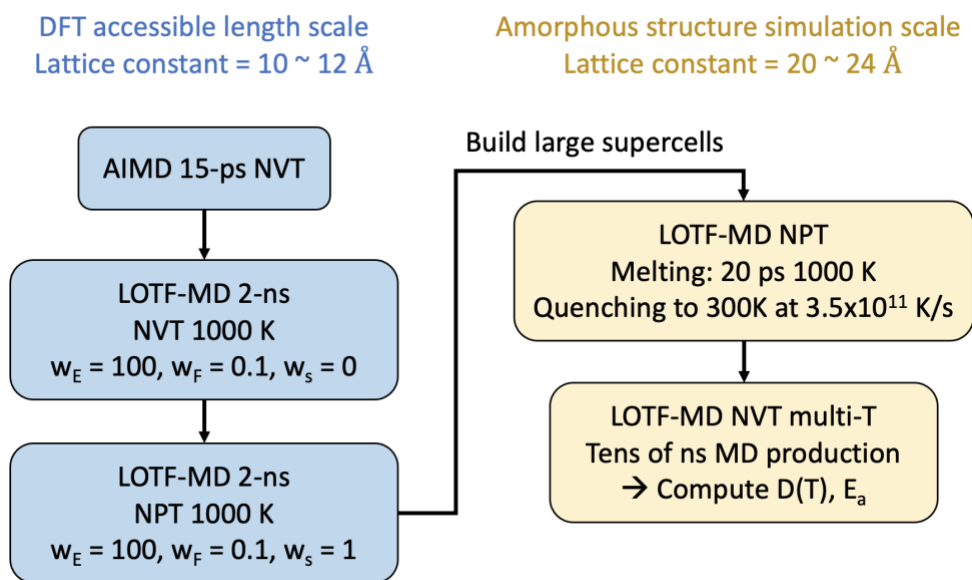
DFT accessible length scale
Lattice constant = 10 ~ 12 Å

Amorphous structure simulation scale
Lattice constant = 20 ~ 24 Å

```
AIMD 15-ps NVT
```

Build large supercells

```
LOTF-MD 2-ns
NVT 1000 K
wE = 100, wF = 0.1, ws = 0
```

```
LOTF-MD NPT
Melting: 20 ps 1000 K
Quenching to 300K at 3.5x10^11 K/s
```

```
LOTF-MD 2-ns
NPT 1000 K
wE = 100, wF = 0.1, ws = 1
```

```
LOTF-MD NVT multi-T
Tens of ns MD production
→ Compute D(T), Ea
```

Figure 1. Potential training and MD production of bulk Li_3PS_4, bulk $Li_3B_{11}O_{18}$ and $Li_3PS_4/Li_3B_{11}O_{18}$ interface: Initial AIMD and learning on-the-fly MD in supercells of 10-12Å, followed by melt-quench in large simulation cells (>20 angstroms between periodic images) to obtain equilibrated amorphous structure models and calculate ionic diffusion coefficients.

Amorphous structures were optimized using the melt-quench method as shown in Figure 1. To generate the initial training dataset for moment tensor potentials[73], an AIMD simulation was carried out for 15 ps at 1000 K in the NVT ensemble. In each AIMD run, the first 2 ps were used for equilibration and then a 13 ps dynamic trajectory was produced for training. The initial training data for the interatomic potential was generated by taking snapshots of the AIMD simulation at intervals of 10 fs. This potential was then used in learning on-the-fly MD (LOTF-MD) at 1000 K until the MD simulation ran for at least 2 ns without activating DFT re-training. Then LOTF-MD simulations in the NPT ensemble were performed at 1000 K for a duration of at least 2 ns to relax the lattice strain. MTP-MD runs in the subsequent iterations were initialized by the last non-extrapolating snapshot from the previous MD run. In this way, the quality of amorphous structures and the potential models were simultaneously improved during LOTF-MD iterations. During MTP learning on-the-fly, the training weights of energy, force, and stresses were 100:0.1:0 and 100:0.1:1 for NVT-MD and NPT-MD, respectively. The ensemble of independently generated training sets, with compositions of Li_3PS_4, $Li_3B_{11}O_{18}$ and $Li_3PS_4/Li_3B_{11}O_{18}$, were consolidated into one training set containing a diverse sampling of local atomic configurations. A single interatomic potential was trained on this combined set of training data. To validate the prediction accuracy of the trained potential and compare the energies of structures generated by LOTF-MD with those from AIMD, we performed AIMD static calculations on 200 snapshots evenly selected from a 2 ns LOTF-MD trajectory with 10 ps time interval for each composition.

To calculate the diffusion properties of the bulk amorphous materials, we constructed 2×2×2 supercells of the final structure from the previous LOTF-MD runs. For the interface, we constructed a 2×2×1 supercell. The supercells contain 1024, 768 and 896 atoms for compositions of Li_3PS_4, $Li_3B_{11}O_{18}$ and $Li_3PS_4/Li_3B_{11}O_{18}$ interface, respectively. The potential trained on the combined training data was used to melt the system at 1000 K in the NPT ensemble for 20 ps, which ensures loss of the memory of the initial configuration. The system was subsequently cooled linearly to 300 K in 2 ns with the cooling rate at 3.5×10^{11} K/s. We then equilibrated the glassy system at 300 K at 1 atm pressure in the NPT ensemble for 1 ns to relax any stress.

We applied the following equation to compute the tracer diffusivity:

$$D_{tr} = \lim_{t \to \infty} \frac{1}{6} \frac{\langle \Delta^2 r(t) \rangle}{t} \tag{1}$$

where $\langle \Delta^2 r(t) \rangle$ is the mean square displacement (MSD) of Li atom after time t, and the constant 6 is used for three-dimensional diffusion. To calculate the tracer diffusivity as a function of temperature, we performed LOTF-MD in the NVT ensemble with the lattice dimension fixed at that of the room-temperature equilibrated structures. The initial temperature (T) for LOTF-MD simulations of each simulation snapshot was 720 K, and the MD simulation temperature was

decremented by 10 K until the diffusivity of Li was so low that no site-to-site hopping was detected within 100 ns. The temperature-dependent diffusivities were used to fit the Arrhenius relationship,

$$D(T) = D(\infty) e^{-\frac{E_a}{k_B T}}. \tag{2}$$

We denote the estimated tracer diffusivity at temperature T as $D(T)$. The activation energy, E_a, can be calculated from a linear fit of $\log(D(T))$ to $\frac{1}{k_B T}$, where k_B is Boltzmann's constant. As demonstrated by He $et\ al.,$[74] the variance of the independent variable D should be considered when fitting the Arrhenius equation for a statistically meaningful estimation of E_a. Following their method, we estimated the variance of the diffusivity of lithium ions and propagated to the variance of the activation energy E_a. These variances were then used in a weighted least-squares regression to estimate E_a. The equation for variance calculation and weighted least-squares regression are provided in Section 1 of the Supplemental Information. The room-temperature conductivity σ_{300K} was calculated using the Nernst−Einstein relation under the assumption that the Haven ratio is equal to one:[75, 76]

$$\sigma_{300K} = \frac{ne^2 z^2}{k_B T} D_{300K}, \tag{3}$$

where n is the volume density of the diffusing species, e is the unit electron charge, z is the charge of the ionic conductor (here 1 for Li$^+$), and D_{300K} is the extrapolated room-temperature tracer diffusivity.

3. Calculation of interfacial energy

The interfacial energy, $\gamma_{interface}$ is computed with respect to the two constituent bulk phases:

$$\gamma_{interface} = \frac{1}{2A}\left(E_{interface} - N_{LBO} E_{LBO} - N_{LPS} E_{LPS} \right), \tag{4}$$

where $E_{interface}$ denotes the total energy the simulated interface model, $E_{bulk,LBO}$ and $E_{bulk,LPS}$ are the energy per formula unit of amorphous Li_3PS_4 and $Li_3B_{11}O_{18}$, respectively, N_{LBO} and N_{LPS} are the number of formula units of $Li_3B_{11}O_{18}$ and Li_3PS_4 in the interface system, and A is the area of each interface in the simulation cell.

Results and discussion
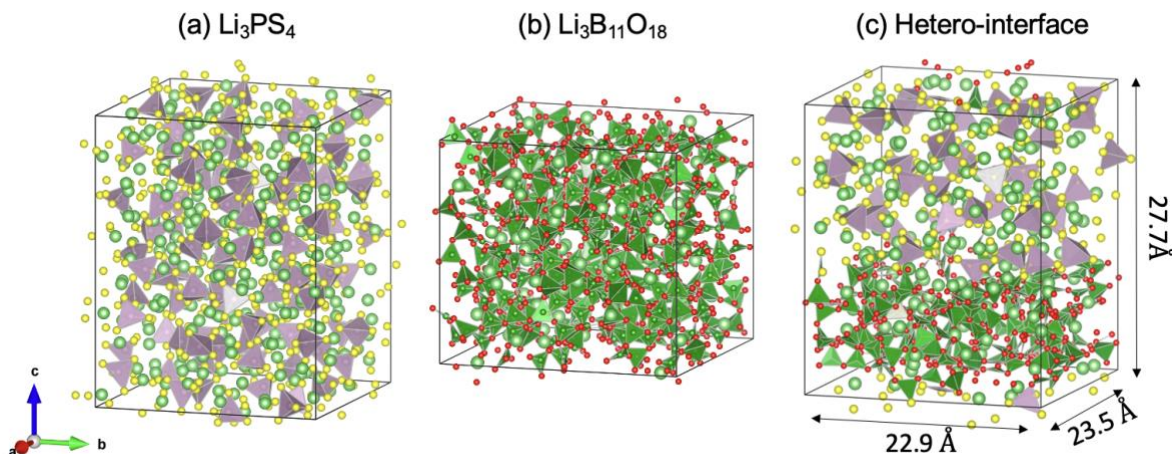
  1. Structure of simulated glasses

Figure 2. Snapshots from LOTF-MD trajectories in the final production steps at 300 K for the amorphous structures of (a) LPS, (b) LBO, and (c) the interface between LPS and LBO. Green, yellow and red spheres represent Li, S and O, respectively. Purple tetrahedra, green tetrahedra and triangles represent PS4, BO4 and BO3 ionic units, respectively. The dimensions of the unit cell used for the interface are shown on the schematic.

We evaluate the atomic ordering in the amorphous structures generated by the melt-quench method (Figure 2) by calculating the pair radial distribution functions (RDFs) of Li-Li, B-O and P-S pairs with reference to their crystalline counterparts (Figure 3). The Li-Li RDF in both bulk materials exhibits no sharp peaks, suggesting a highly disordered Li distribution in the glasses at room temperature. In contrast, the clear peaks in the P-S and B-O pair distribution functions indicates that the PS4 tetrahedra, BO4 tetrahedra and BO3 triangular anion units remain largely intact in the amorphous structures during Li diffusion (Figure 3). Our computed RDF of amorphous Li3PS4 agrees with previous experimental characterization where the first peak around 2.0 Å is due to the P–S covalent bond in PS_4^{3-} which are the predominant anion units in the structure.[77] The RDF of non-lithium species in the amorphous structures differ from crystals in the longer range features. Integrating the curves for P-S and B-O pairs (Figure 3) up to the first minimum (~2.5Å), the average coordination number of P by S atoms and B by O atoms are 4 and 3.2, respectively. A similar analysis was conducted on the geometry of interfaces, and approximately the same coordination number of P-S and B-O were obtained. This suggests that the short-range ordering of anion units in the interface resembles that in the bulk phase.
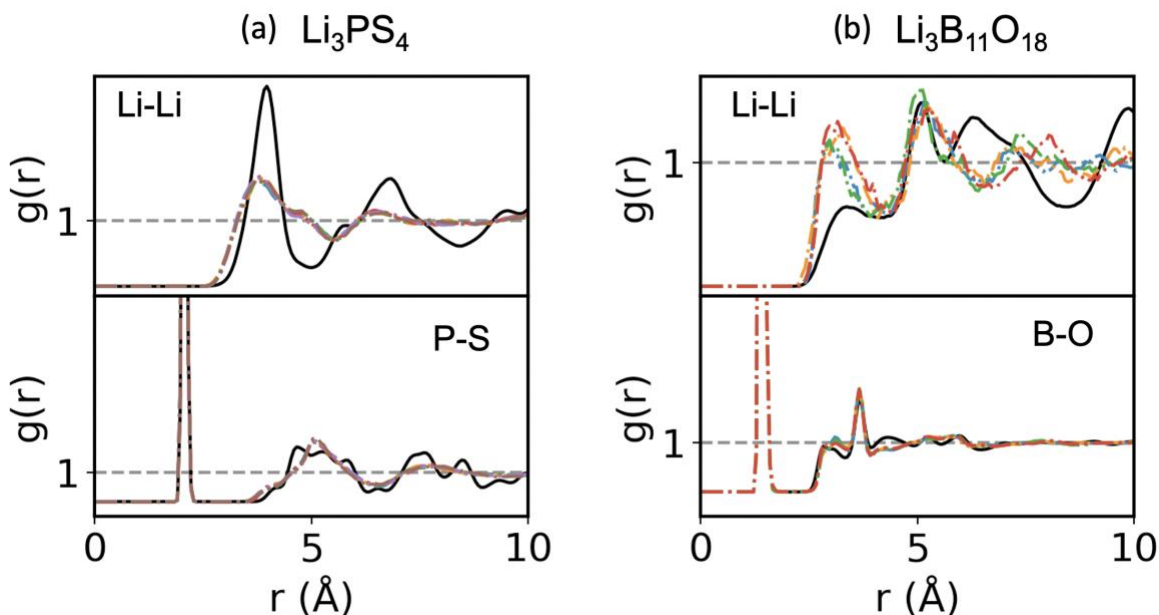
Figure 3. Pair radial distribution functions (RDFs) at 300 K of (a) amorphous Li_3PS_4 for atom pairs Li-Li and P-S, and (b) amorphous $Li_3B_{11}O_{18}$ for atom pairs Li-Li and B-O with reference to their crystalline counterparts. Colored dash lines represent the RDFs from LOTF-MD trajectories of multiple independently simulated amorphous structures. Black solid lines represent the RDFs of crystalline Li_3PS_4 and crystalline $Li_3B_{11}O_{18}$.

The thermal history of glasses is critical to the structural properties of amorphous systems.[78, 79] However, given the timescale accessible to AIMD, which are generally less than a nanosecond, the simulated cooling rate in an AIMD simulation is typically on the order of 10^{13}-10^{15} K/s, which is much higher than that performed experimentally (1–100 K/s).[80-82] Several computational studies have investigated the effect of thermal history on the structures and properties of silicate, borate, phosphate, borosilicate and aluminosilicate glasses.[83-86] It was found that cooling rates in the range of 5×10^{12} - 1×10^{11} K/s yield reasonable structural properties.[79, 87, 88] Enabled by the high efficiency of LOTF-MD, we carry out cooling over 2 ns time duration at the rate of 3.5×10^{11} K/s, which would be prohibitively expensive with AIMD in large unit cells.

To better understand the effects of cooling rate on the amorphous structure we compare the radial distribution functions produced by cooling at 3.5×10^{11} K/s with those produced by fast quenching at 3.5×10^{14} K/s (Figure 4). The fast quenching rate resulted in considerably more spread in the pair distributions functions than the quenching rate that was three orders of magnitude slower, suggesting that the pair distributions functions had not yet converged. This provides evidence that high quenching rates might result in unrealistic structures in the amorphous system, which highlights the important role of active learning potential models in studies of amorphous materials. Although additional structural refinement might be achieved with even slower quenching, convergence of the cation spatial distribution among multiple MD initializations indicates that the simulated quenching provides a reasonable approximation to the actual amorphous structure. It

has previously been reported that intermolecular S-S units can emerge from fast quenching.[89] An RDF analysis of S-S pairs (SI Figure S1) in our samples shows a similar peak for intermolecular S-S bond formation at the fast cooling rate, but the peak is not apparent at the slow cooling rate.
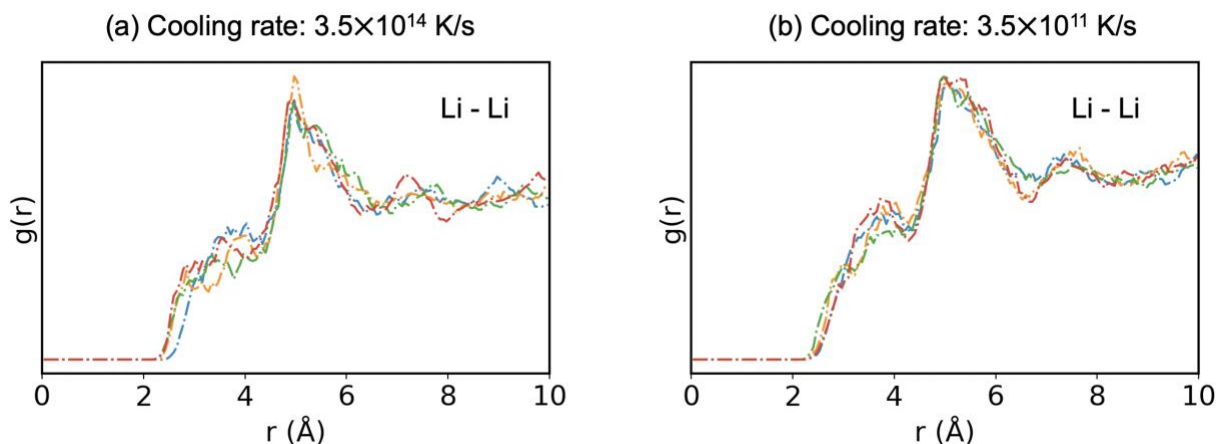

Figure 4. Li-Li pair radial distribution functions (RDFs) of glass $Li_3B_{11}O_{18}$ at 300 K in configurations produced by cooling at the rate of a) 3.5×10^{14} K/s b) 3.5×10^{11} K/s.
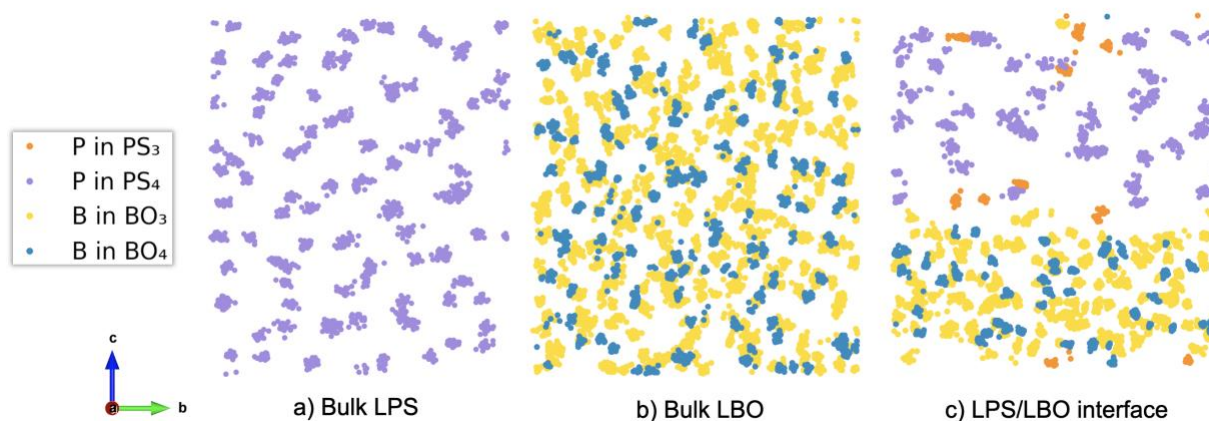
Figure 5. Trajectories of B and P atoms during 20 ns LOTF-MD at 700 K in the unit cell projected on the b-c plane for a) bulk LPS b) bulk LBO and c) a LPS/LBO interface. Coordination environments of B and P atoms are colored according to the legend.

For the interface structures, most of the time a clear boundary between the two materials can be recognized, while occasionally B-O units diffuse into the solid electrolyte. There are two types of polyhedra (BO_3 and BO_4) in the lithium borate glassy network. To investigate the arrangement of the polyatomic anions at the interface, we analyze the coordination numbers of boron with oxygen and phosphorus with sulfur over the course of 20 ns of LOTF-MD production. As shown in the

trajectory plot (Figure 5), the distribution of polyatomic anions in the bulk materials is similar to that near the interface. The molar fraction of BO_4 tetrahedra with reference to the total number of B-O units (0.26) is slightly higher than the molar fraction in the unit cells containing an interface (0.22).

To validate the generated structures (Figure 2 and Supplemental Information Figure S2), we compared the calculated densities to those previously reported in literature. The density of Li_3PS_4 relaxed by LOTF-MD in the NPT ensemble at room temperature is 1.79 ± 0.014 g/cm^3 averaged over four independent simulation cells. Experimental measurements of the density vary between 1.45 and 1.89 depending on the molding conditions.[90] The AIMD-calculated density of LPS glasses, calculated using melt-quench procedures, have been reported as 1.79 g/cm^3 and 1.56 g/cm^3.[37, 91] In the paper reporting the lower density,[37] it was suggested that the difference might be attributed to fact that the computational cell was constrained to be cubic in the calculation that yielded the higher density.[37] To clarify this discrepancy, we performed AIMD in the NPT ensemble following the procedures in ref [37] where a density of 1.56 g/cm^3 was reported, and we obtained a density of 1.802 g/cm^3 after 30 ps AIMD. The density evolution over the course of AIMD simulation is shown in the SI Figure S3. This indicates that LOTF-MD reproduces the AIMD optimized density well. The LOTF-MD-calculated density averaged over an ensemble of four $Li_3B_{11}O_{18}$ is 2.09 ± 0.01 g/cm^3, which achieves good agreement with the experimental density of 2.1 g/cm^3.[92, 93]

2. Energies of amorphous bulk materials and interfaces

To calculate the energies of bulk amorphous materials and interfaces, the initial atomic structure of each amorphous phase at room temperature was obtained using the melt-quench procedures described in the Methods section. To examine the progress of energy minimization and geometry optimization over time, we took snapshots evenly selected from the trajectories of the initial AIMD (150 fs time interval), LOTF-MD equilibration (10 ps time interval), and production periods (10 ps time interval) and recalculated their energies by DFT to make a comparison with AIMD. We note that across all systems, the mean absolute validation error between DFT and MTP is about 4 meV / atom (Figure 6) and 0.24 eV/Å (Figure S4) for energies and forces, respectively. To understand the evolution of the structure over time, we also calculate the Global Instability Index (GII) of these snapshots. The GII represents the mean deviation of the bond valence sums from the formal valences.[94] It has been previously used to evaluate the stability of crystalline structures,[95, 96] and here we use it as a measure of atomic order in amorphous structures. The procedure of calculating the GII can be found in Section 2 of the Supplemental Information.

From MD trajectories of bulk glasses and the amorphous interface structures, we found a substantial correlation between GII and the DFT energy which continuously decreased over the course of the initial AIMD period and the LOTF-MD equilibration period. In Figure 7, we illustrate this trend for the solid-solid amorphous interface structure, which possesses the highest degree of complexity among the systems we studied. During the initial 15 ps AIMD simulation, the energy decreased from -5.74 eV/atom to -5.99 eV/atom, and the GII decreased from 0.6 to 0.4. In the

subsequent 100 ps LOTF-MD equilibration, the total energy further decreased by 0.1 eV/atom. This suggests that inadequate equilibration time (e.g. tens of picoseconds) could yield structures trapped in unrealistically high energy states. In the final LOTF-MD production, the GII ranged from 0.24 to 0.33, and the total energy fluctuated between -6.11 eV/atm and -6.13 eV/atom, which suggests the convergence of energy. As a reference, it has generally been found that stable crystalline structures are characterized by GII $\leq$ 0.2,[94, 97, 98] suggesting that the amorphous structures exist just outside this range.
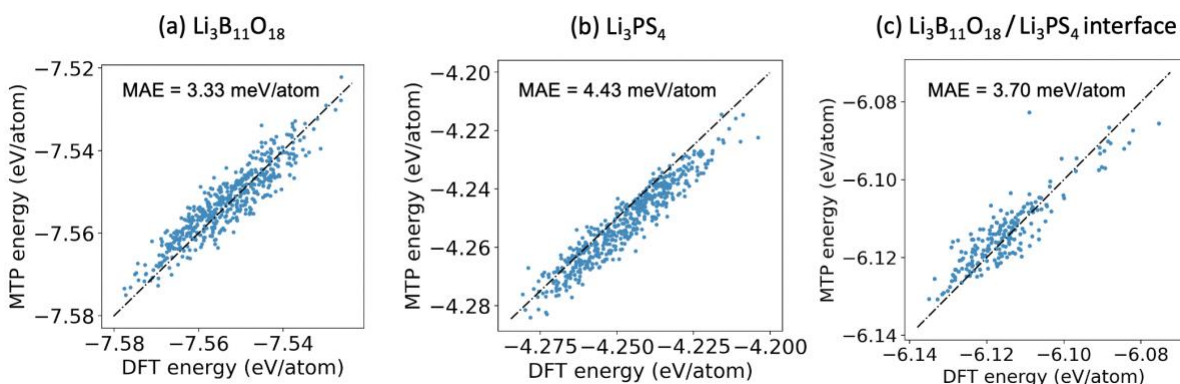
Figure 6. Comparison of DFT- and MTP-predicted energies for snapshots selected from 2 ns LOTF-MD trajectories for a) bulk $Li_3B_{11}O_{18}$, b) bulk Li_3PS_4 and c) the $Li_3B_{11}O_{18}/$ Li_3PS_4 interface. The corresponding mean absolute errors (MAE) are labeled on the plots.
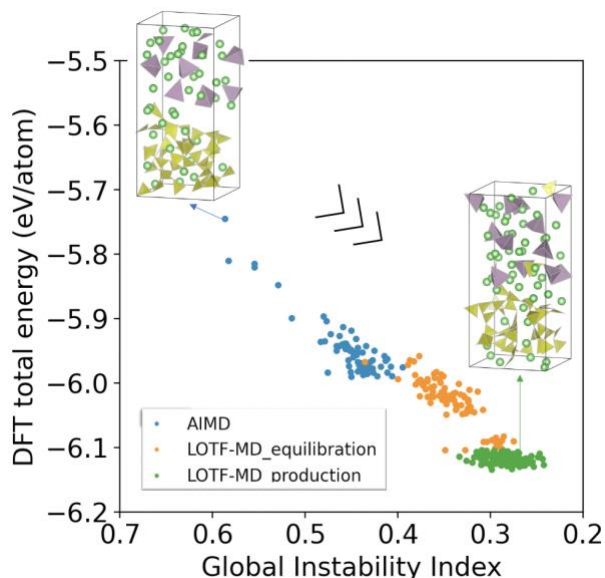

Figure 7. DFT energy per atom of an interface structure plotted against the global instability index (GII) for 13 ps AIMD started from randomly initialized structure (blue), 100 ps LOTF-MD equilibration (orange), and 1 ns LOTF-MD production (green). The configurations at the first step of AIMD and the last step of LOTF-MD production are shown on the plot.

The energies of bulk Li_3PS_4, bulk $Li_3B_{11}O_{18}$, and the interface are determined by taking the ensemble average of structures in the LOTF-MD production period for each composition. Based on the DFT energies of amorphous Li_3PS_4 and $Li_3B_{11}O_{18}$ with reference to their crystalline counterparts, we calculated the amorphization energies to be 36.7 and 42.0 meV/atom, respectively. These values are on the lower end of the range of amorphization energies reported in a systematic study of 41 binary amorphous systems by AIMD.[93] This is consistent with the strong glass forming tendency of these materials and the long equilibration times enabled by LOTF-MD. The relatively slow cooling rate allowed the structures to relax into low-energy amorphous configurations that may be impractical to achieve with AIMD, ultimately yielding more physically plausible and representative models for subsequent structural and dynamic analyses.

The interfacial energy between the two amorphous phases (Equation (4)) was calculated to be 620 mJ/m^2 (38.5 $meV/Å^2$). To our knowledge, this is the first time the interfacial energy between two amorphous ionic compounds has been reported. This is just above the range of a typical semicoherent interface (200 – 500 mJ/m^2) and comparable to that of a low-energy incoherent interface.[99] For comparison, the computationally predicted interfacial energies of crystalline $LiCO_2/\beta$- Li_3PS_4[54] and Li/γ- Li_3PO_4[52] have been reported to be 2466 and 624 mJ/m^2, respectively.

3. Li-ion conductivity of bulk and interfacial amorphous systems

To accurately characterize the transport properties of lithium ions in the glass materials and minimize finite-size effects, we constructed supercells of over 2 nm in each dimension for bulk Li_3PS_4 and $Li_3B_{11}O_{18}$. Figure 8(a) and (b) show the calculated total Li^+ temperature-dependent diffusivities of the sulfide and borate glasses, where the Arrhenius relationship is fitted to statistics collected from multiple uncorrelated amorphous phases. The error bar on each averaged diffusivity data point is derived from hundreds of nanoseconds MD trajectories using the method of He *et al.*[74] At intermediate temperatures for systems with activation energies over 0.5 eV, a nano-to-micro second timescale is essential to obtain results with high statistical quality. While there are varying diffusivities at the same temperature among the different samples (especially in the borate), the average diffusivities exhibit good linear dependence on reciprocal temperature for both the fast-conducting sulfide electrolyte and the intermediate-conducting borate coating. The statistical quality is enhanced by the extensive sampling of the configuration space by nanosecond timescale LOTF-MD production.
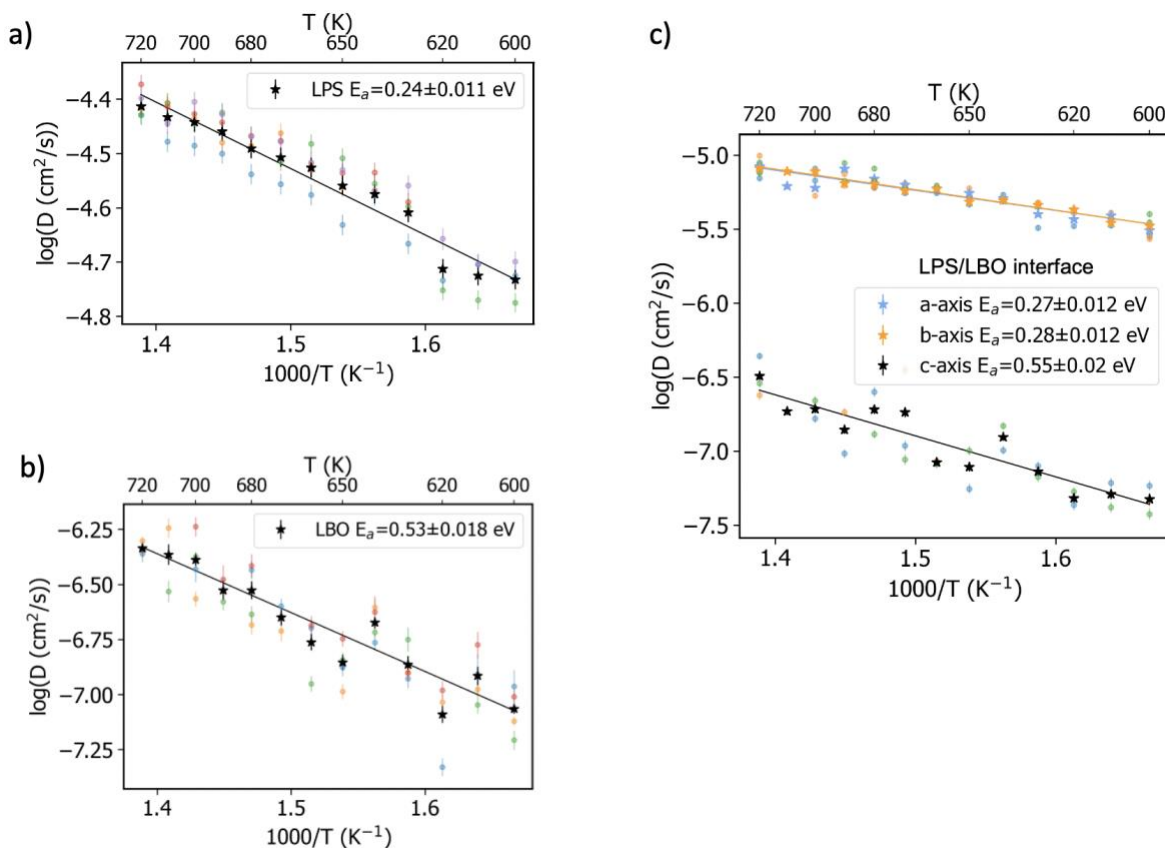
Figure 8. Arrhenius plots of Li$^+$ temperature-dependent diffusivities and activation energies (Ea) for bulk (a) Li$_3$PS$_4$ (b) Li$_3$B$_{11}$O$_{18}$, and (c) Li$_3$PS$_4$/ Li$_3$B$_{11}$O$_{18}$ diffusion along the three main axes. Each series of colored dots represents an independently simulated glass structure. At each temperature, an average diffusivity is calculated across all of these structures as shown by the black stars with corresponding error bars. The weighted Arrhenius fit to the diffusion data is denoted by the black lines.

The calculated bulk Li$_3$PS$_4$ conductivity is 16.4×10^{-3} S cm^{-1} at 300 K, in good agreement with 19×10^{-3} S cm^{-1} from a comprehensive study of Li$_3$PS$_4$ using AIMD.[37] The theoretical predicted ionic conductivities are higher than experimentally characterized values by about two order of magnitude.[100-102] It has been speculated that ionic-impeding impurity/residues such as Li$_2$S, P$_2$S$_6^{4-}$ and P$_2$S$_7^{4-}$ raised the apparent Li-ion diffusion barrier in the synthesized amorphous Li$_3$PS$_4$.[37]

The conductivity for Li$_3$B$_{11}$O$_{18}$ calculated using LOTF-MD is 1.38×10^{-4} S cm^{-1} at 300 K with a predicted diffusion activation energy of 0.53 eV. We have not found any reported experimentally-determined ionic conductivity for this specific borate glass in the literature. For comparison, the experimental activation energy for the composition 0.2Li$_2$O·0.8B$_2$O$_3$ with a lower Li content is 0.8 eV.[103]

To probe the impact of the interface on the ionic conductivity across the cell, we analyze diffusivities along axes parallel and perpendicular to the interface plane as shown in Figure 8(c). The lateral isotropic diffusion barrier represents the total resistance of bulk sulfide glass, borate glass, and the interface connected in parallel. The apparent activation energy is dominated by the component with the highest ionic conductivity. In the direction normal to the interface, lithium ions encounter the resistance of the bulk sulfide glass, the interface and the borate glass connected in series. In this direction, the activation energy is dominated by the component that has lowest ionic conductivity.

To ensure sufficient sampling of all three types of diffusion, we analyzed the displacement of each individual lithium ion along interface normal as shown in Figure 9. The distance between neighboring interfaces in the simulation cell is ~14 Å. The histogram shows that within 1 ns MD production, most lithium ions were bouncing within the bulk phases and few diffusion hops across the interface were sampled. During the long MD simulation of 55 ns, over 25% of the lithium ions in the simulation cell have displaced from their original location by at least 30 Å in the direction normal to the interface, which means they have traveled across an interface at least two times.

To determine the extent to which the amorphous-amorphous interface may hinder lithium ion conductivity in a solid-state battery, we compare the diffusion across the interface to diffusion in the bulk materials. If the interface were a significant barrier to diffusivity, we would expect to see a significantly higher activation energy for diffusion in the direction normal to the interface. However the calculated activation energy in this direction (0.55±0.02 eV) is very similar to the calculated activation energy for diffusion through the bulk borate glass (0.53±0.02 eV), giving evidence that diffusion across the interface does not reduce the rate of Li-ion conduction. These findings are in line with previous studies demonstrating that the local Li-ion environment has minimal impact on Li-ion diffusivity.[35, 89] Our results indicate that lithium ions experience negligible additional impedance when diffusing between amorphous sulfide and borate anion sublattice. This might not be the case with crystalline systems due to lattice mismatch at the interface.
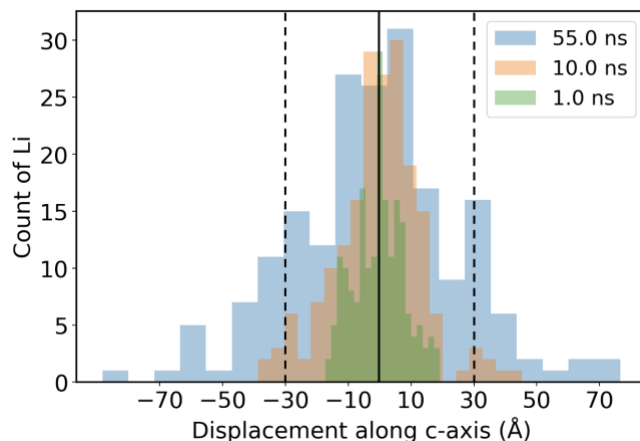
Figure 9. Histogram showing the displacement of lithium ions along the *c* axis perpendicular to the interface averaged over four individual interface structures simulated at 700 K for durations of 1 ns, 10 ns, and 55 ns.
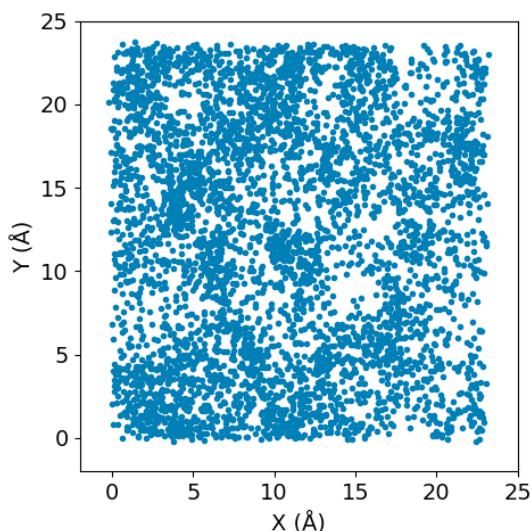

Figure 10. Trajectory of interface-crossing Li atoms projected onto the x-y plane.

To investigate the diffusion pathways across the amorphous interface, we calculated an isosurface of Li-ion probability density for the LPS/LBO interface at 700 K (Supplementary Information Figure S4(a)). In addition, we calculated the distribution of lithium ions moving across the interface by keeping track of lithium ions coordinated by both S (from Li_3PS_4) and O (from $Li_3B_{11}O_{18}$) atoms excluding those coordinated by both S and O atoms in the snapshot taken 1 ps earlier. The spatial distribution plots in Figure 10 and Figure S5 provide evidence for a homogeneous distribution of Li diffusion events within the interface region, with some fluctuations in density at the angstrom scale that are likely due to the host atomic structure.

Conclusions

Machine-learned interatomic potentials trained on-the-fly with DFT can give new insights into the kinetic behavior of amorphous materials and interfaces. Through realistic large-scale MD simulations using a highly accurate machine-learned interatomic potential model, we investigated the interface morphology, thermodynamic properties, and Li-ion diffusion rates in amorphous battery materials. We found that the amorphous structures obtained by simulated melt-and-quench are critically affected by the cooling rate, and AIMD in particular may be insufficiently fast to obtain a reasonable approximation of the amorphous structure. With MD simulations of tens of nanoseconds enabled by the machine-learned potential model, we obtained structures with amorphization energies significantly lower than those obtained by sub-nanosecond quenching. The structural stability of these amorphous structures as measured by the global instability index is just above the range of crystalline materials. The interfacial energy between the sulfide solid electrolyte and borate protective coating was calculated to be 620 mJ/m^2, which to our knowledge is the first calculation of the interfacial energy between two amorphous materials from first principles. The calculated activation energies for lithium-ion diffusion across the interface provide quantitative evidence that the interface between amorphous Li_3PS_4 and amorphous $Li_3B_{11}O_{18}$ does not impede Li-ion diffusion. The method introduced in this study is generalizable to model a variety of interfaces involving amorphous materials, which can help to reduce experimental efforts of synthesizing and characterizing these systems.

Supporting Information

Details of statistical error analysis and weighted Arrhenius fitting; Global instability index (GII) calculation method; Radial distribution function (RDF) analysis of S-S pairs in the glass structure simulated by two different cooling rates; Snapshots of simulated glasses; The density evolution over 30 ps AIMD simulation of amorphous Li_3PS_4; Mean absolute errors for predictions of forces by MTP with reference to DFT; Isosurfaces of the Li-ion probability density distribution from the LOTF-MD simulation at 700 K for the LPS/LBO interface and spatial distribution of interface-crossing Li atoms.

Acknowledgement

References

1.   Goodenough, J. B.; Park, K. S., The Li-ion rechargeable battery: a perspective. *J Am Chem Soc* **2013,** *135* (4), 1167-76.

2.   Janek, J.; Zeier, W. G., A solid future for battery development. *Nat Energy* **2016,** *1* (9), 1-6.

3.   Manthiram, A.; Yu, X.; Wang, S., Lithium battery chemistries enabled by solid-state electrolytes. *Nature Reviews Materials* **2017,** *2* (4), 1-16.

4.   Kamaya, N.; Homma, K.; Yamakawa, Y.; Hirayama, M.; Kanno, R.; Yonemura, M.; Kamiyama, T.; Kato, Y.; Hama, S.; Kawamoto, K.; Mitsui, A., A lithium superionic conductor. *Nat Mater* **2011,** *10* (9), 682-6.

5.   Zhu, Y. Z.; He, X. F.; Mo, Y. F., Origin of Outstanding Stability in the Lithium Solid Electrolyte Materials: Insights from Thermodynamic Analyses Based on First-Principles Calculations. *Acs Appl Mater Inter* **2015,** *7* (42), 23685-23693.

6.   Kim, J. G.; Son, B.; Mukherjee, S.; Schuppert, N.; Bates, A.; Kwon, O.; Choi, M. J.; Chung, H. Y.; Park, S., A review of lithium and non-lithium based solid state batteries. *J Power Sources* **2015,** *282*, 299-322.

7.   Auvergniot, J.; Cassel, A.; Ledeuil, J. B.; Viallet, V.; Seznec, V.; Dedryvere, R., Interface Stability of Argyrodite Li6PS5Cl toward LiCoO2, LiNi1/3Co1/3Mn1/3O2, and LiMn2O4 in Bulk All-Solid-State Batteries. *Chem Mater* **2017,** *29* (9), 3883-3890.

8.   Tian, Y. S.; Shi, T.; Richards, W. D.; Li, J. C.; Kim, J. C.; Bo, S. H.; Ceder, G., Compatibility issues between electrodes and electrolytes in solid-state batteries. *Energ Environ Sci* **2017,** *10* (5), 1150-1166.

9.   Zhu, Y. Z.; He, X. F.; Mo, Y. F., First principles study on electrochemical and chemical stability of solid electrolyte-electrode interfaces in all-solid-state Li-ion batteries. *J Mater Chem A* **2016,** *4* (9), 3253-3266.

10.   Pervez, S. A.; Cambaz, M. A.; Thangadurai, V.; Fichtner, M., Interface in Solid-State Lithium Battery: Challenges, Progress, and Outlook. *ACS Appl Mater Interfaces* **2019,** *11* (25), 22029-22050.

11.   Richards, W. D.; Miara, L. J.; Wang, Y.; Kim, J. C.; Ceder, G., Interface Stability in Solid-State Batteries. *Chem Mater* **2015,** *28* (1), 266-273.

12.   Nolan, A. M.; Zhu, Y.; He, X.; Bai, Q.; Mo, Y., Computation-Accelerated Design of Materials and Interfaces for All-Solid-State Lithium-Ion Batteries. *Joule* **2018,** *2* (10), 2016-2046.

13.   Curtarolo, S.; Hart, G. L.; Nardelli, M. B.; Mingo, N.; Sanvito, S.; Levy, O., The high-throughput highway to computational materials design. *Nat Mater* **2013,** *12* (3), 191-201.

14.   Van der Ven, A., Lithium Diffusion in Layered Li[sub x]CoO[sub 2]. *Electrochemical and Solid-State Letters* **1999,** *3* (7), 301.

15.   Ong, S. P.; Wang, L.; Kang, B.; Ceder, G., Li-Fe-P-O-2 phase diagram from first principles calculations. *Chemistry of Materials* **2008,** *20* (5), 1798-1807.

16.   Xiao, Y.; Miara, L. J.; Wang, Y.; Ceder, G., Computational Screening of Cathode Coatings for Solid-State Batteries. *Joule* **2019,** *3* (5), 1252-1275.

17.   He, X.; Zhu, Y.; Mo, Y., Origin of fast ion diffusion in super-ionic conductors. *Nat Commun* **2017,** *8*, 15893.

18.   Shi, S.; Lu, P.; Liu, Z.; Qi, Y.; Hector, L. G., Jr.; Li, H.; Harris, S. J., Direct calculation of Li-ion transport in the solid electrolyte interphase. *J Am Chem Soc* **2012,** *134* (37), 15476-87.

19.   Urban, A.; Seo, D.-H.; Ceder, G., Computational understanding of Li-ion batteries. *npj Computational Materials* **2016,** *2* (1), 1-13.

20.   Bachman, J. C.; Muy, S.; Grimaud, A.; Chang, H. H.; Pour, N.; Lux, S. F.; Paschos, O.; Maglia, F.; Lupart, S.; Lamp, P.; Giordano, L.; Shao-Horn, Y., Inorganic Solid-State Electrolytes for Lithium Batteries: Mechanisms and Properties Governing Ion Conduction. *Chem Rev* **2016,** *116* (1), 140-62.

21.   Xiong, F.; Tao, H.; Yue, Y., Role of Amorphous Phases in Enhancing Performances of Electrode Materials for Alkali Ion Batteries. *Frontiers in Materials* **2020,** *6*, 328.

22.   Grady, Z. A.; Wilkinson, C. J.; Randall, C. A.; Mauro, J. C., Emerging Role of Non-crystalline Electrolytes in Solid-State Battery Research. *Front Energy Res* **2020,** *8*, 218.

23.   Islam, M. M.; Bredow, T.; Heitjans, P., The ionic conductivity in lithium-boron oxide materials and its relation to structural, electronic and defect properties: insights from theory. *J Phys Condens Matter* **2012,** *24* (20), 203201.

24.   Ohta, N.; Takada, K.; Zhang, L. Q.; Ma, R. Z.; Osada, M.; Sasaki, T., Enhancement of the high-rate capability of solid-state lithium batteries by nanoscale interfacial modification. *Adv Mater* **2006,** *18* (17), 2226-+.

25.   Ohta, N.; Takada, K.; Sakaguchi, I.; Zhang, L.; Ma, R.; Fukuda, K.; Osada, M.; Sasaki, T., LiNbO3-coated LiCoO2 as cathode material for all solid-state lithium secondary batteries. *Electrochem Commun* **2007,** *9* (7), 1486-1490.

26.   Jung, S. H.; Oh, K.; Nam, Y. J.; Oh, D. Y.; Brüner, P.; Kang, K.; Jung, Y. S., Li3BO3–Li2CO3: Rationally Designed Buffering Phase for Sulfide All-Solid-State Li-Ion Batteries. *Chem Mater* **2018,** *30* (22), 8190-8200.

27.   Woo, J. H.; Travis, J. J.; George, S. M.; Lee, S.-H., Utilization of Al2O3Atomic Layer Deposition for Li Ion Pathways in Solid State Li Batteries. *J Electrochem Soc* **2014,** *162* (3), A344-A349.

28.   Sakuda, A.; Kitaura, H.; Hayashi, A.; Tadanaga, K.; Tatsumisago, M., All-solid-state lithium secondary batteries with oxide-coated LiCoO2 electrode and Li2S–P2S5 electrolyte. *J Power Sources* **2009,** *189* (1), 527-530.

29.   Okumura, T.; Takeuchi, T.; Kobayashi, H., All-solid-state lithium-ion battery using Li2.2C0.8B0.2O3 electrolyte. *Solid State Ionics* **2016,** *288*, 248-252.

30.   Zhang, Y. Q.; Tian, Y.; Xiao, Y.; Miara, L. J.; Aihara, Y.; Tsujimura, T.; Shi, T.; Scott, M. C.; Ceder, G., Direct Visualization of the Interfacial Degradation of Cathode Coatings in Solid State Batteries: A Combined Experimental and Computational Study. *Advanced Energy Materials* **2020,** *10* (27).

31.   Sastre, J.; Futscher, M. H.; Pompizi, L.; Aribia, A.; Priebe, A.; Overbeck, J.; Stiefel, M.; Tiwari, A. N.; Romanyuk, Y. E., Blocking lithium dendrite growth in solid-state batteries with an ultrathin amorphous Li-La-Zr-O solid electrolyte. *Communications Materials* **2021,** *2* (1), 1-10.

32.   Hayashi, A.; Hama, S.; Morimoto, H.; Tatsumisago, M.; Minami, T., Preparation of Li2S–P2S5 amorphous solid electrolytes by mechanical milling. *Journal of the American Ceramic Society* **2001,** *84* (2), 477-79.

33.   Balaish, M.; Gonzalez-Rosillo, J. C.; Kim, K. J.; Zhu, Y.; Hood, Z. D.; Rupp, J. L., Processing thin but robust electrolytes for solid-state batteries. *Nat Energy* **2021,** *6* (3), 227-239.

34.   Hirata, A., Local structure analysis of amorphous materials by angstrom-beam electron diffraction. *Microscopy (Oxf)* **2021,** *70* (2), 171-177.

35.   Lee, B.; Jun, K.; Ouyang, B.; Ceder, G., Weak Correlation between the Polyanion Environment and Ionic Conductivity in Amorphous Li–P–S Superionic Conductors. *Chem Mater* **2023,** *35* (3), 891-899.

36.   Zheng, Z.; Fang, H.; Yang, F.; Liu, Z.-K.; Wang, Y., Amorphous LiLaTiO3 as solid electrolyte material. *J Electrochem Soc* **2014,** *161* (4), A473.

37.   Smith, J. G.; Siegel, D. J., Low-temperature paddlewheel effect in glassy solid electrolytes. *Nat Commun* **2020,** *11* (1), 1483.

38.   Varsamis, C.-P. E.; Vegiri, A.; Kamitsos, E. I., Molecular dynamics investigation of lithium borate glasses: Local structure and ion dynamics. *Phys Rev B* **2002,** *65* (10), 104203.

39.   Stechert, T.; Rushton, M.; Grimes, R.; Dillon, A., Predicted structure, thermo-mechanical properties and Li ion transport in LiAlF4 glass. *Journal of non-crystalline solids* **2012,** *358* (16), 1917-1923.

40.   Biswas, P.; Atta-Fynn, R.; Drabold, D., Reverse Monte Carlo modeling of amorphous silicon. *Phys Rev B* **2004,** *69* (19), 195207.

41.   McGreevy, R. L., Reverse monte carlo modelling. *Journal of Physics: Condensed Matter* **2001,** *13* (46), R877.

42.   Botu, V.; Ramprasad, R., Adaptive machine learning framework to accelerate ab initio molecular dynamics. *Int J Quantum Chem* **2015,** *115* (16), 1074-1083.

43.   Mueller, T.; Hernandez, A.; Wang, C., Machine learning for interatomic potential models. *The Journal of Chemical Physics* **2020,** *152* (5), 050902.

44.   Sendek, A. D.; Cubuk, E. D.; Antoniuk, E. R.; Cheon, G.; Cui, Y.; Reed, E. J., Machine Learning-Assisted Discovery of Solid Li-Ion Conducting Materials. *Chem Mater* **2019,** *31* (2), 342-352.

45.   Guo, H.; Wang, Q.; Stuke, A.; Urban, A.; Artrith, N., Accelerated Atomistic Modeling of Solid-State Battery Materials With Machine Learning. *Front Energy Res* **2021,** *9*, 695902.

46.   Wang, C.; Aoyagi, K.; Wisesa, P.; Mueller, T., Lithium Ion Conduction in Cathode Coating Materials from On-the-Fly Machine Learning. *Chem Mater* **2020,** *32* (9), 3741-3752.

47.   Wang, C.; Aoyagi, K.; Aykol, M.; Mueller, T., Ionic Conduction through Reaction Products at the Electrolyte-Electrode Interface in All-Solid-State Li(+) Batteries. *ACS Appl Mater Interfaces* **2020,** *12* (49), 55510-55519.

48.   Wang, C.; Aoyagi, K.; Mueller, T., Computational design of double-layer cathode coatings in all-solid-state batteries. *J Mater Chem A* **2021,** *9* (Issue 40, 2021), 23206-23213.

49.   Atkins, D.; Ayerbe, E.; Benayad, A.; Capone, F. G.; Capria, E.; Castelli, I. E.; Cekic-Laskovic, I.; Ciria, R.; Dudy, L.; Edström, K.; Johnson, M. R.; Li, H.; Lastra, J. M. G.; De Souza, M. L.; Meunier, V.; Morcrette, M.; Reichert, H.; Simon, P.; Rueff, J. P.; Sottmann, J.; Wenzel, W.; Grimaud, A., Understanding Battery Interfaces by Combined Characterization and Simulation Approaches: Challenges and Perspectives. *Advanced Energy Materials* **2021**, 2102687.

50.   Sicolo, S.; Fingerle, M.; Hausbrand, R.; Albe, K., Interfacial instability of amorphous LiPON against lithium: A combined Density Functional Theory and spectroscopic study. *J Power Sources* **2017,** *354*, 124-133.

51.   Han, X.; Gong, Y.; Fu, K. K.; He, X.; Hitz, G. T.; Dai, J.; Pearse, A.; Liu, B.; Wang, H.; Rubloff, G.; Mo, Y.; Thangadurai, V.; Wachsman, E. D.; Hu, L., Negating interfacial impedance in garnet-based solid-state Li metal batteries. *Nat Mater* **2017,** *16* (5), 572-579.

52.   Lepley, N. D.; Holzwarth, N. A. W., Modeling interfaces between solids: Application to Li battery materials. *Phys Rev B* **2015,** *92* (21), 214201.

53.   Sumita, M.; Tanaka, Y.; Ikeda, M.; Ohno, T., Charged and Discharged States of Cathode/Sulfide Electrolyte Interfaces in All-Solid-State Lithium Ion Batteries. *The Journal of Physical Chemistry C* **2016,** *120* (25), 13332-13339.

54.   Gao, B.; Jalem, R.; Ma, Y.; Tateyama, Y., Li+ Transport Mechanism at the Heterogeneous Cathode/Solid Electrolyte Interface in an All-Solid-State Battery via the First-Principles Structure Prediction Scheme. *Chem Mater* **2019,** *32* (1), 85-96.

55.   Henkelman, G.; Uberuaga, B. P.; Jonsson, H., A climbing image nudged elastic band method for finding saddle points and minimum energy paths. *Journal of Chemical Physics* **2000,** *113* (22), 9901-9904.

56.   Henkelman, G.; Jonsson, H., Improved tangent estimate in the nudged elastic band method for finding minimum energy paths and saddle points. *Journal of Chemical Physics* **2000,** *113* (22), 9978-9985.

57.   Perdew, J. P.; Emzerhof, M.; Burke, K., Rationale for mixing exact exchange with density functional approximations. *Journal of Chemical Physics* **1996,** *105* (22), 9982-9985.

58.   Blochl, P. E., Projector Augmented-Wave Method. *Physical Review B* **1994,** *50* (24), 17953-17979.

59.   Kresse, G.; Furthmuller, J., Efficient iterative schemes for ab initio total-energy calculations using a plane-wave basis set. *Phys Rev B Condens Matter* **1996,** *54* (16), 11169-11186.

60.   Kresse, G.; Joubert, D., From ultrasoft pseudopotentials to the projector augmented-wave method. *Physical Review B* **1999,** *59* (3), 1758-1775.

61.   Ong, S. P.; Mo, Y. F.; Richards, W. D.; Miara, L.; Lee, H. S.; Ceder, G., Phase stability, electrochemical stability and ionic conductivity of the Li10 +/- 1MP2X12 (M = Ge, Si, Sn, Al or P, and X = O, S or Se) family of superionic conductors. *Energy & Environmental Science* **2013,** *6* (1), 148-156.

62.   Zhu, Z. Y.; Chu, I. H.; Ong, S. P., Li3Y(PS4)(2) and Li5PS4Cl2: New Lithium Superionic Conductors Predicted from Silver Thiophosphates using Efficiently Tiered Ab Initio Molecular Dynamics Simulations. *Chemistry of Materials* **2017,** *29* (6), 2474-2484.

63.   Hoover, W. G., Canonical dynamics: Equilibrium phase-space distributions. *Phys Rev A Gen Phys* **1985,** *31* (3), 1695-1697.

64.   Nosé, S., A unified formulation of the constant temperature molecular dynamics methods. *The Journal of Chemical Physics* **1984,** *81* (1), 511-519.

65.   Parrinello, M.; Rahman, A., Polymorphic transitions in single crystals: A new molecular dynamics method. *Journal of Applied Physics* **1981,** *52* (12), 7182-7190.

66.   Parrinello, M.; Rahman, A., Crystal Structure and Pair Potentials: A Molecular-Dynamics Study. *Physical Review Letters* **1980,** *45* (14), 1196-1199.

67.   Plimpton, S., Fast Parallel Algorithms for Short-Range Molecular Dynamics. *J. Comput. Phys.* **1995,** *117* (1), 1-19.

68.   Settles, B., *Active learning literature survey*. Computer Sciences Technical Report 1648, University of Wisconsin-Madison: 2010.

69.   Podryabinkin, E. V.; Shapeev, A. V., Active learning of linearly parametrized interatomic potentials. *Comp Mater Sci* **2017,** *140*, 171-180.

70.   Hoover, W. G., Canonical dynamics: Equilibrium phase-space distributions. *Physical review A* **1985,** *31* (3), 1695.

71.   Homma, K.; Yonemura, M.; Kobayashi, T.; Nagao, M.; Hirayama, M.; Kanno, R., Crystal structure and phase transitions of the lithium ionic conductor Li3PS4. *Solid State Ionics* **2011,** *182* (1), 53-58.

72.   Sennova, N.; Albert, B.; Bubnova, R.; Krzhizhanovskaya, M.; Filatov, S., Anhydrous lithium borate, Li3B11O18, crystal structure, phase transition and thermal expansion. *Zeitschrift für Kristallographie - Crystalline Materials* **2014,** *229* (7), 497-504.

73.   Shapeev, A. V., Moment Tensor Potentials: A Class of Systematically Improvable Interatomic Potentials. *Multiscale Modeling & Simulation* **2016,** *14* (3), 1153-1173.

74.   He, X.; Zhu, Y.; Epstein, A.; Mo, Y., Statistical variances of diffusional properties from ab initio molecular dynamics simulations. *npj Computational Materials* **2018,** *4* (1), 18.

75.   Marcolongo, A.; Marzari, N., Ionic correlations and failure of Nernst-Einstein relation in solid-state electrolytes. *Phys Rev Mater* **2017,** *1* (2), 025402.

76.   de Klerk, N. J. J.; van der Maas, E.; Wagemaker, M., Analysis of Diffusion in Solid-State Electrolytes through MD Simulations, Improvement of the Li-Ion Conductivity in beta-Li3PS4 as an Example. *ACS Appl Energy Mater* **2018,** *1* (7), 3230-3242.

77.   Shiotani, S.; Ohara, K.; Tsukasaki, H.; Mori, S.; Kanno, R., Pair distribution function analysis of sulfide glassy electrolytes for all-solid-state batteries: Understanding the improvement of ionic conductivity under annealing condition. *Sci Rep* **2017,** *7* (1), 6972.

78.   Varshneya, A. K., *Fundamentals of inorganic glasses*. Elsevier: 2013; p 37-69.

79.   Vollmayr, K.; Kob, W.; Binder, K., Cooling-rate effects in amorphous silica: A computer-simulation study. *Phys Rev B* **1996,** *54* (22), 15808.

80.   Car, R.; Parrinello, M., Structural, dymanical, and electronic properties of amorphous silicon: an ab initio molecular-dynamics study. *Physical review letters* **1988,** *60* (3), 204.

81.   Stich, I.; Car, R.; Parrinello, M., Amorphous silicon studied by ab initio molecular dynamics: Preparation, structure, and properties. *Physical review. B, Condensed matter* **1991,** *44* (20), 11092-11104.

82.   Cooper, N.; Goringe, C.; McKenzie, D., Density functional theory modelling of amorphous silicon. *Comp Mater Sci* **2000,** *17* (1), 1-6.

83.   Deng, L.; Du, J., Development of effective empirical potentials for molecular dynamics simulations of the structures and properties of boroaluminosilicate glasses. *Journal of Non-Crystalline Solids* **2016,** *453*, 177-194.

84.   Kieu, L.-H.; Delaye, J.-M.; Cormier, L.; Stolz, C., Development of empirical potentials for sodium borosilicate glass systems. *Journal of non-crystalline solids* **2011,** *357* (18), 3313-3321.

85.   Ganster, P.; Benoit, M.; Kob, W.; Delaye, J.-M., Structural properties of a calcium aluminosilicate glass from molecular-dynamics simulations: A finite size effects study. *The Journal of chemical physics* **2004,** *120* (21), 10172-10181.

86.   Malavasi, G.; Pedone, A.; Menziani, M. C., Study of the structural role of gallium and aluminum in 45S5 bioactive glasses by molecular dynamics simulations. *The Journal of Physical Chemistry B* **2013,** *117* (15), 4142-4150.

87.   Li, X.; Song, W.; Yang, K.; Krishnan, N. M. A.; Wang, B.; Smedskjaer, M. M.; Mauro, J. C.; Sant, G.; Balonis, M.; Bauchy, M., Cooling rate effects in sodium silicate glasses: Bridging the gap between molecular dynamics simulations and experiments. *J Chem Phys* **2017,** *147* (7), 074501.

88. Deng, L.; Du, J., Effects of system size and cooling rate on the structure and properties of sodium borosilicate glasses from molecular dynamics simulations. *J Chem Phys* **2018,** *148* (2), 024504.

89. Sadowski, M.; Albe, K., Computational study of crystalline and glassy lithium thiophosphates: Structure, thermodynamic stability and transport properties. *J Power Sources* **2020,** *478*.

90. Sakuda, A.; Hayashi, A.; Takigawa, Y.; Higashi, K.; Tatsumisago, M., Evaluation of elastic modulus of $Li_2S–P_2S_5$ glassy solid electrolyte by ultrasonic sound velocity measurement and compression test. *J Ceram Soc Jpn* **2013,** *121* (1419), 946-949.

91. Baba, T.; Kawamura, Y., Structure and Ionic Conductivity of Li2S–P2S5 Glass Electrolytes Simulated with First-Principles Molecular Dynamics. *Front Energy Res* **2016,** *4*.

92. Lelong, G.; Cormier, L.; Hennet, L.; Michel, F.; Rueff, J.-P.; Ablett, J. M.; Monaco, G., Lithium borate crystals and glasses: How similar are they? A non-resonant inelastic X-ray scattering study around the B and O K-edges. *Journal of Non-Crystalline Solids* **2017,** *472*, 1-8.

93. Wright, A. C.; Feller, S. A.; Hannon, A. C., *Borate glasses, crystals & melts*. Society of glass technology: 1997.

94. Salinas-Sanchez, A.; Garcia-Muñoz, J. L.; Rodriguez-Carvajal, J.; Saez-Puche, R.; Martinez, J. L., Structural characterization of R2BaCuO5 (R = Y, Lu, Yb, Tm, Er, Ho, Dy, Gd, Eu and Sm) oxides by X-ray and neutron diffraction. *J Solid State Chem* **1992,** *100* (2), 201-211.

95. Zhang, H.; Li, N.; Li, K.; Xue, D., Structural stability and formability of ABO3-type perovskite compounds. *Acta Crystallogr B* **2007,** *63* (Pt 6), 812-8.

96. Thangadurai, V.; Adams, S.; Weppner, W., Crystal Structure Revision and Identification of Li+-Ion Migration Pathways in the Garnet-like Li5La3M2O12 (M = Nb, Ta) Oxides. *Chem Mater* **2004,** *16* (16), 2998-3006.

97. Brown, I., Modelling the structures of La2NiO4. *Zeitschrift für Kristallographie* **1992,** *199* (3-4), 255-272.

98. Armbruster, T.; Roethlisberger, F.; Seifert, F., Layer topology, stacking variation, and site distortion in melilite-related compounds in the system CaO-ZnO-GeO2-SiO2. *American Mineralogist* **1990,** *75* (7-8), 847-858.

99. Porter, D., KE Easterling Phase transformations in metals and alloys. 2nd edition ed.; Chapman & Hall, London: 1992; pp 144-147.

100. Ohara, K.; Mitsui, A.; Mori, M.; Onodera, Y.; Shiotani, S.; Koyama, Y.; Orikasa, Y.; Murakami, M.; Shimoda, K.; Mori, K.; Fukunaga, T.; Arai, H.; Uchimoto, Y.; Ogumi, Z., Structural and electronic features of binary Li(2)S-P(2)S(5) glasses. *Sci Rep* **2016,** *6*, 21302.

101. Hayashi, A.; Hama, S.; Morimoto, H.; Tatsumisago, M.; Minami, T., Preparation of Li2S-P2S5 Amorphous Solid Electrolytes by Mechanical Milling. *Journal of the American Ceramic Society* **2004,** *84* (2), 477-79.

102. Dietrich, C.; Weber, D. A.; Sedlmaier, S. J.; Indris, S.; Culver, S. P.; Walter, D.; Janek, J.; Zeier, W. G., Lithium ion conductivity in Li2S–P2S5 glasses – building units and local structure evolution during the crystallization of superionic conductors Li3PS4, Li7P3S11 and Li4P2S7. *J Mater Chem A* **2017,** *5* (34), 18111-18119.

103. Montouillout, V.; Fan, H.; del Campo, L.; Ory, S.; Rakhmatullin, A.; Fayon, F.; Malki, M., Ionic conductivity of lithium borate glasses and local structure probed by high resolution solid-sate NMR. *Journal of Non-Crystalline Solids* **2018,** *484*, 57-64.

SUPPORTING INFORMATION

Nature of the amorphous-amorphous interfaces in solid-state batteries revealed using machine-learned interatomic potentials

Chuhong Wang,[1] Muratahan Aykol,[2] Tim Mueller[1,*]

[1]Materials Science and Engineering, John Hopkins University, Baltimore, MD, USA, 21218
[2]Toyota Research Institute

Corresponding author: Tim Mueller tmueller@jhu.edu

Table of Contents

1. Statistical error analysis and weighted Arrhenius fitting

He, X. F. *et al.*, defined the relative standard deviation as the ratio between the standard deviation of the diffusivity and the diffusivity itself.[1] Through a series of benchmarks they fit the following equation for the relative standard deviation (RSD) of ionic diffusivities:

$$RSD = \frac{s_D}{D_{true}} = \frac{3.43}{\sqrt{N_{eff}}} + 0.04 \tag{1}$$

where

$$N_{eff} = \frac{\max_{\Delta t}\left[\mathrm{TMSD}(\Delta t)\right]}{a^2} \tag{2}$$

where $\mathrm{TMSD}(\Delta t)$ is the total mean squared displacement (the sum of the mean squared displacements of the lithium atoms) after time Δt and a is the length of a site-to-site ion hop.

To estimate the uncertainty in the calculated activation energies we start from the Arrhenius equation

$$D(T) = D_0 e^{-\frac{E_a}{k_B T}} \tag{3}$$

where $D(T)$ is the diffusivity at temperature T, D_0 is the diffusivity in the limit of infinite temperature, and E_a is the activation energy for diffusion. Taking the natural log of both sides gives an equation that is linear in E_a:

$$\ln\big(D(T)\big) = \ln\big(D_0\big) - \frac{E_a}{k_B T} \tag{4}$$

The variance of $\ln\big(D(T)\big)$, $s^2_{\ln(D(T))}$, is approximately related to the variance in $D(T)$, $\sigma^2_{D_T}$, through the following equation:[2]

$$\sigma^2_{\ln(D(T))} \approx \frac{\sigma^2_{D_T}}{D_T^{\,2}} \tag{5}$$

where we estimate $s^2_{D_T}$ using the equation of He, X. F., et al.[1] (Equation (1) Δt). We estimate E_a by performing a weighted least squares regression[3] of $\ln\big(D(T)\big)$ with respect to $\frac{1}{k_B T}$, where the

3

weight of each sample is the inverse of $\sigma^2_{\ln(D(T))}$ for that sample. E_a is a coefficient of the linear estimator, and the variance of E_a is taken as the square of the standard error of the coefficient. The weighted least squares regression and standard error of the coefficient were calculated using the SciPy package.[4]

2. Global instability index (GII) calculation

The bond valence S_{ij} (the term is associated with cation–anion interaction) of the bond formed between two oppositely charged ions i and j is defined as follows:

$$S_{ij} = exp\left(\frac{R_{ij}^0 - R_{ij}}{b}\right) \tag{1}$$

where R_{ij}^0 is the bond valence parameter of cation–anion pairs, which is empirically determined using experimental room temperature structure data. The value of b can often be treated as a universal constant with a value of $0.37.$[5] The bond valence sum of the i th ion is represented as follows:

$$V_{i(cal)} = \sum S_{ij} \tag{2}$$

The bond discrepancy factor d_i is defined as the deviation of the bond valence sum from the formal valence. It is represented as follows:

$$d_i = V_{i(cal)} - V_{i(ox)} \tag{3}$$

where $V_{i(ox)}$ represents the formal valence of the ith ion. The parameter d_i is a measure of bond strain. The global instability index can be expressed as

$$GII = \left\{ \frac{\left[\sum_{i=1}^{N} d_i^2\right]}{N} \right\}^{\frac{1}{2}} \tag{4}$$

where N is the number of ions per unit cell. The further the bond valence sums are from the formal valence of the ion, the greater the value of the GII.

5

Figure S1: RDF analysis of S-S pairs in the glass LPS/LBO interface structure simulated at two different cooling rates: slow cooling at 3.5×10^{14} K/s and fast cooling at 3.5×10^{11} K/s. As reported by M. Sadowski and K. Albe,[6] intermolecular (S−S) bonding will lead to a second peak located around 4 Å.
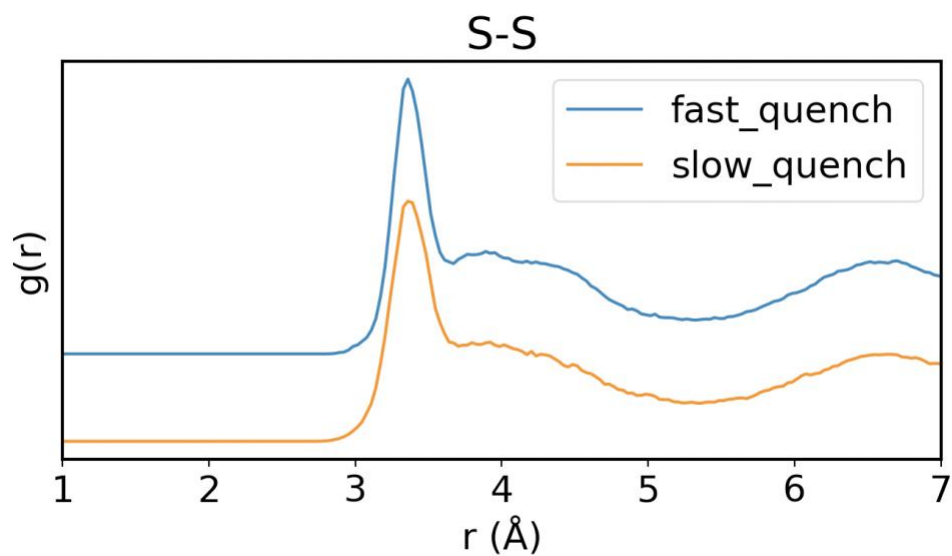

6

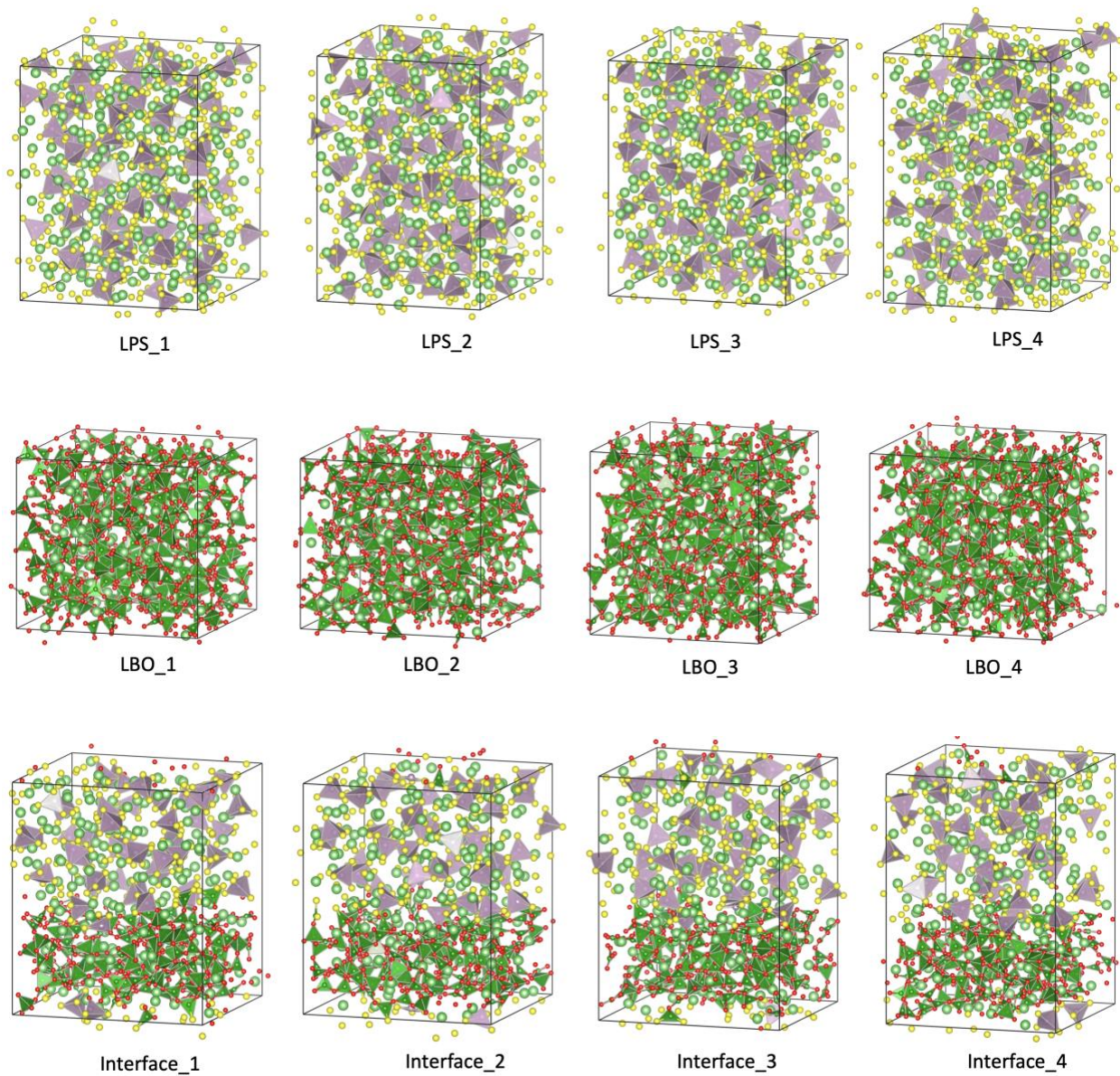**Figure S2:** Snapshots of simulated glass materials and heterogeneous interfaces.

LPS_1   LPS_2   LPS_3   LPS_4

LBO_1   LBO_2   LBO_3   LBO_4

Interface_1   Interface_2   Interface_3   Interface_4

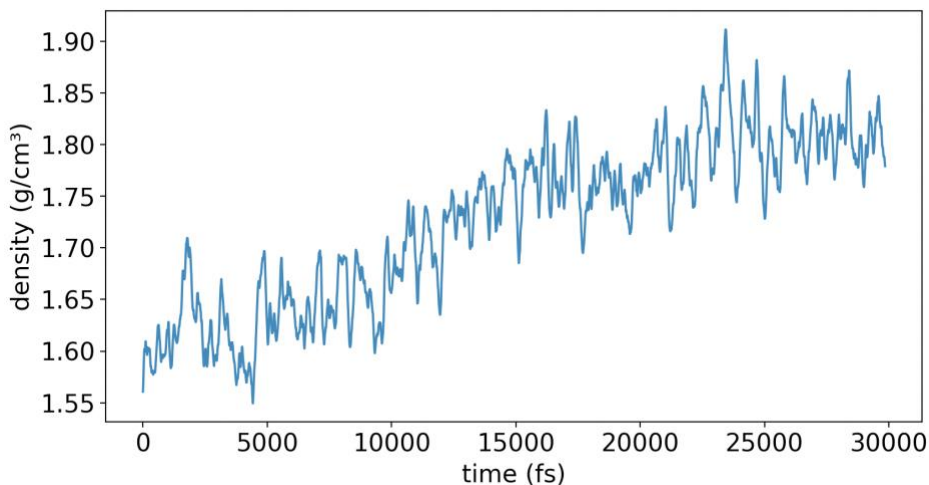**Figure S3:** The density evolution over 30 ps AIMD simulation of amorphous Li_3PS_4

Figure S4: Comparison of DFT- and MTP-predicted forces for snapshots selected from 2 ns LOTF-MD trajectories at 300 K for a) bulk $Li_3B_{11}O_{18}$, b) bulk Li_3PS_4 and c) the $Li_3B_{11}O_{18}/Li_3PS_4$ interface. The corresponding mean absolute errors (MAE) are labeled on the plots.
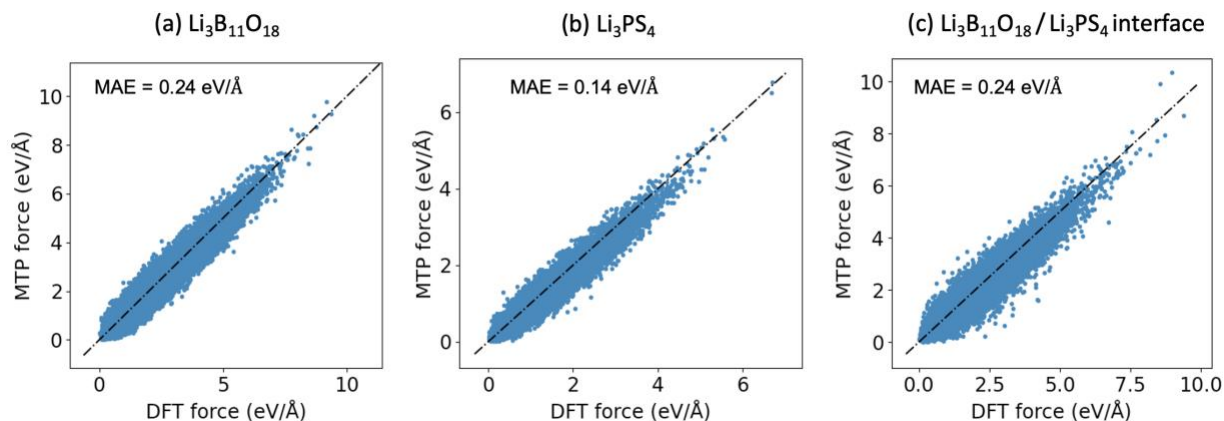
Figure S5: (a) Isosurfaces of the Li-ion probability density distribution from the LOTF-MD simulation at 700 K for LPS/LBO interface. Violet and green polyhedra are the P atoms coordinated by S and B atoms coordinated by O, respectively. (b) Trajectory of interface-crossing Li atoms which are coordinated by both S (from Li_3PS_4) and O (from $Li_3B_{11}O_{18}$) atoms excluding those coordinated by both S and O atoms in the snapshot taken 1 ps earlier.
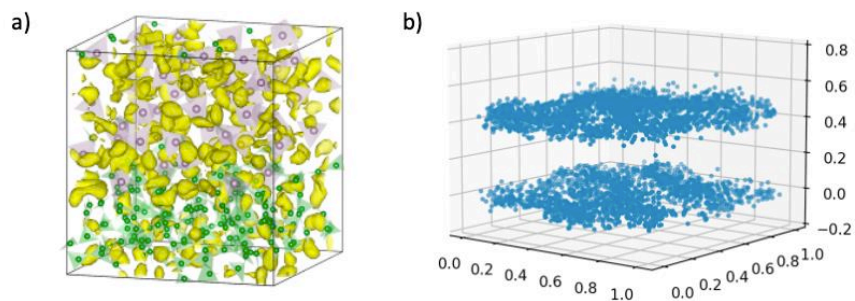
References Cited

1.   He, X.; Zhu, Y.; Epstein, A.; Mo, Y., Statistical variances of diffusional properties from ab initio molecular dynamics simulations. *npj Computational Materials* **2018,** *4* (1), 18.

2.   Liu, X., *Survival Analysis*. 2012.

3.   Pattengill, M. D.; Sands, D. E., Statistical Significance of Linear Least-Squares Parameters. *J Chem Educ* **1979,** *56* (4), 244-247.

4.   Jones, E.; Oliphant, T.; Peterson, P.; others SciPy: Open Source Scientific Tools for Python. https://docs.scipy.org.

5.   Lufaso, M. W.; Woodward, P. M., Prediction of the crystal structures of perovskites using the software program SPuDS. *Acta Crystallogr B* **2001,** *57* (Pt 6), 725-38.

6.   Sadowski, M.; Albe, K., Computational study of crystalline and glassy lithium thiophosphates: Structure, thermodynamic stability and transport properties. *J Power Sources* **2020,** *478*.